MRI Signal Reconstruction via Fourier Frames on Interleaving Spirals
Final Report

Christiana Sabett
Applied Mathematics, Applied Statistics, & Scientific Computation

Advisors: John Benedetto, Alfredo Nava-Tudela
Mathematics, IPST

May 13, 2016

1 Abstract

This project aims to effectively reconstruct an MRI signal using Fourier frames via nonuniform spiral sampling. We begin by describing the theoretical framework of a Fourier frame on the Paley-Wiener space $PW_{\overline{B(0,R)}}$. We then invoke Beurling's theorem to prove that we can choose points along interleaving Archimedean spirals in the spectral domain to construct a Fourier frame for $PW_{\overline{B(0,R)}}$. We use frame notation to extend the result to the signal space of a rectangular image, forming a reconstruction algorithm that results in an overdetermined linear system. We implement two different algorithms to solve the least-squares approximation in order to recover the spatial components of the MRI signal. Preliminary results from a synthetic data set are presented.

2 Background

MRI signal reconstruction from spectral sampling is a common problem in the field of signal processing. Formally stated, image reconstruction is an inversion problem: given frequency information, we want to recover the spatial components of the image. MRI reconstruction in particular desires both speed and accuracy, but often the former is neglected. Previous results have shown that sampling on interleaving spirals in the spectral domain makes for much faster data acquisition than rectilinear spectral sampling [6, 9]. We desire a reconstruction scheme that makes use of this data acquisition method. The standard approach to MRI reconstruction relies on uniform sampling of the spectral domain [12]. When sampling nonuniformly, classic reconstruction schemes still require the samples be mapped to a uniform grid. We will show that by sampling nonuniformly along the interleaving spirals, we can construct a Fourier frame approximant that allows us to achieve effective MRI reconstruction comparable to that recovered from uniform sampling.

It is well-established that uniform sampling in the spectral domain of a band-limited signal can produce perfect reconstruction, where the reconstructed signal is a scaled, delayed version of the original signal. The Nyquist theorem states that a band-limited signal must be sampled at a rate at least twice the maximum frequency in order to achieve this reconstruction [12]. Rectilinear sampling in the spectral domain consists of points (λ, μ) where $\lambda = mh_\lambda$ and $\mu = nh_\mu$ for $m, n \in \mathbb{Z}$ and for fixed distances between coordinates h_λ and h_μ that satisfy the Nyquist criterion. The typical MRI reconstruction algorithm samples rectilinearly and then applies the Fast Fourier Transform (FFT) to recover the image [7, 12].

A standard MRI machine measures the exact spectral components of the signal. Coils generate a magnetic field that causes the body's particles to align with it along a magnetic vector. The charged particles rotate about the static magnetic field B_0, typically oriented in the z direction, at the Larmor frequency ω_0, creating

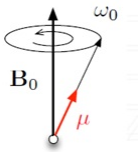

Figure 2.1: Magnetic dipole moment μ. Image courtesy of Alfredo Nava-Tudela.

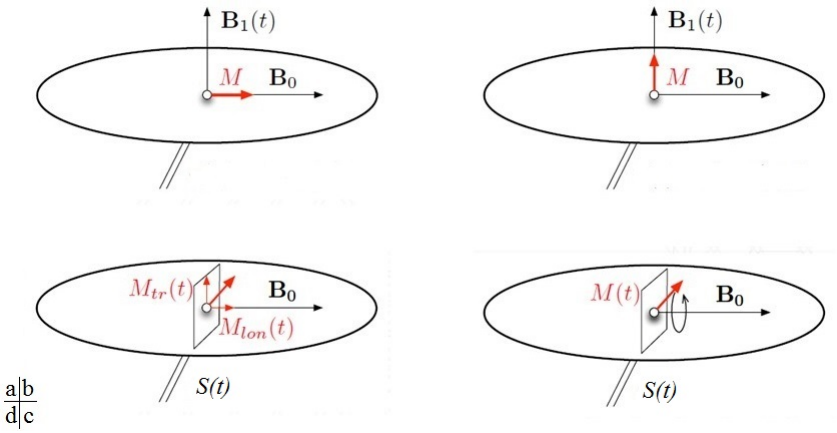

Figure 2.2: MRI process. Clockwise from top left: a. Local magnetization M emerges from alignment with magnetic field B_0. b. With an RF pulse at the Larmor frequency, M aligns with the magnetic field B_1 in the transversal plane. c. After the pulse, M begins to realign with B_0. d. Components $M_{lon}(t)$ and $M_{tr}(t)$ describe $M(t)$ at time t. Images courtesy of Alfredo Nava-Tudela.

a magnetic dipole moment μ. The Larmor frequency is proportional to the strength of the magnetic field B_0 at gyromagnetic ratio γ. When the majority of the magnetic moments align with B_0, a local magnetization of the sample M is observed. A radio wave frequency (RF) is then passed through the body to disrupt the magnetic field, forcing the particles out of equilibrium and generating a magnetic field B_1 perpendicular to B_0, oscillating at frequency ω. When $\omega = \omega_0$, the magnetization M moves to the transversal plane. Once the pulse passes, M rotates around B_0, eventually realigning with it. The magnetization vector $M(t)$ is defined by its components in the longitudinal (B_0) direction $M_{lon}(t)$ and the transversal (B_1) direction $M_{tr}(t)$ at time t. The magnetization components $M_{lon}(t)$ and $M_{tr}(t)$ decay exponentially proportional to relaxation times T_1 and T_2, respectively, as described by Bloch's seminal equations [5].

When the RF pulse passes, an induced voltage $S(t)$ is observed in the transversal plane related to the $M_{tr}(t)$ component of the magnetization. This voltage is the measured signal. When viewed in the transversal (xy) plane, $M(t)$ decays in a spiral. The induced voltage $S(t)$ can be described relative to the gradient of B_0 in k-space with the observed decay pattern.

$$\begin{aligned} S(t) = S(k(t)) &= S(k_x(t), k_y(t), k_z(t)) \\ &= \int\int\int M_{tr}(x,y,z) e^{-2\pi i \langle (x,y,z)(k_x,k_y,k_z)\rangle} dxdydz \\ &= \int\int\int \rho(x,y,z) e^{-t/T_2} e^{-2\pi i \langle (x,y,z)(k_x(t),k_y(t),k_z(t))\rangle} dxdydz \end{aligned}$$

Here, $\rho(x,y,z)$ is the density of the tissue and for $r = x, y, z$,

$$k_r(t) \propto \int_0^t \frac{\delta}{\delta r} B_0(u) du$$

Overall, we see that the signal S is proportional to the transversal component of the magnetization M in magnetic gradient space, allowing for the recovery of an image of M_{tr} via an inverse Fourier transform of S.

$$S(k) \propto \int M_{tr} e^{-2\pi i \mathbf{k}\cdot\mathbf{r}} d\mathbf{V}$$

Analysis of the signal shows that the time it takes for the particles to return to homeostasis and the amount of energy released indicate the type of tissue the pulses are moving through [4, 13].

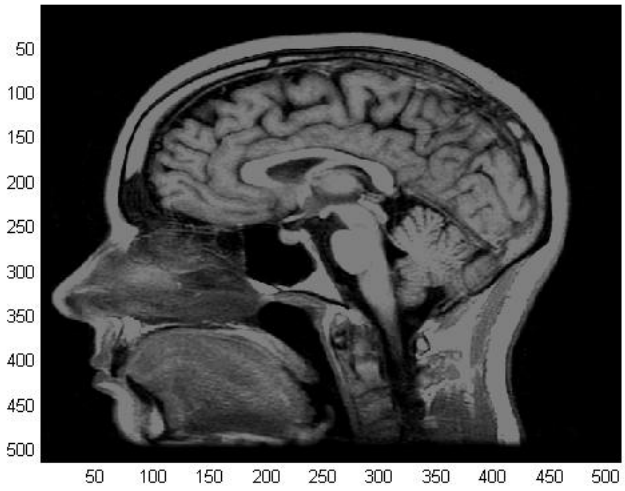

Figure 2.3: "Carolyn's MRI", by ClintJCL (Flickr)

Spiral-scan echo planar imaging (SEPI) designs magnetic gradients to sample S at points in k-space that form Archimedean spirals [9]. Typically, S is sampled 256 times, but the design is constrained by the relaxation time T_2. We will show that with added constraints as dictated by Beurling, we can recover images such as Figure 2.3 with comparable quality from samples along interleaving Archimedean spirals.

3 Theoretical Approach

The *Paley-Wiener space* PW_E is defined as

$$PW_E = \{\varphi \in L^2(\widehat{\mathbb{R}}^d) : \text{supp } \varphi^\vee \subseteq E\},$$

where $\widehat{\mathbb{R}}^d$ is the domain of the Fourier transforms of signals in d-dimensional Euclidean space, and $L^2(\widehat{\mathbb{R}}^d)$ is the space of finite energy signals on $\widehat{\mathbb{R}}^d$ with $E \subseteq \mathbb{R}^d$ compact. The Fourier transform of a signal $f(x)$ is defined as $\mathcal{F} : L^2(\mathbb{R}^d) \to L^2(\widehat{\mathbb{R}}^d)$ such that $\mathcal{F}(f)(\omega) = \int_{-\infty}^{\infty} f(x) e^{-2\pi i x\cdot\omega} dx$. $\varphi^\vee$ denotes the inverse Fourier transform of φ and supp $\varphi^\vee$ denotes the support of $\varphi^\vee$ [3].

In a separable Hilbert space H, a *frame* is defined as a sequence $\{x_n : n \in \mathbb{Z}^d\} \subseteq H$ for which there exist $A, B > 0$ such that

$$\forall y \in H, \quad A||y||^2 \leq \sum_n |\langle y, x_n\rangle|^2 \leq B||y||^2.$$

Let $\Lambda \subseteq \widehat{\mathbb{R}}^d$ be a sequence and let $E \subseteq \mathbb{R}^d$ be compact. Define the sequence $\{e_\lambda \mathbb{1}_E : \lambda \in \Lambda\} \subseteq L^2(\mathbb{R}^d)$, where $e_\lambda(x) = e^{-2\pi i x\cdot\lambda}$. In particular, note that $(e_\lambda \mathbb{1}_E)^\wedge \in PW_E$ and $L^2(E) = (PW_E)^\vee$. The sequence $\{e_\lambda \mathbb{1}_E\}$ is a frame for $L^2(E)$, where we write $L^2(E) \subseteq L^2(\mathbb{R}^d)$ because $(PW_E)^\vee \subseteq L^2(\mathbb{R}^d)$, if and only if there exist $0 < A \leq B < \infty$ such that

$$\forall f \in L^2(E), \quad A||f||^2_{L^2(E)} \leq \sum_{\lambda\in\Lambda} |\langle f, e_\lambda \mathbb{1}_E\rangle_{L^2(E)}|^2 \leq B||f||^2_{L^2(E)}$$

where $\langle f, e_\lambda \mathbb{1}_E \rangle_{L^2(E)} = \int_E f(x) e^{-2\pi i x \cdot \lambda} dx = \widehat{f}(\lambda)$. We can further say that the sequence $(e_\lambda \mathbb{1}_E)^\wedge$ is a frame for PW_E if $\{e_\lambda \mathbb{1}_E\}$ is a frame for $L^2(E)$. We call such a sequence a *Fourier frame for* PW_E [1, 3].

A set Λ is *uniformly discrete* if there exists $r > 0$ such that

$$\forall \lambda, \gamma \in \Lambda, \quad |\lambda - \gamma| \geq r.$$

When E is the closed ball $\overline{B(0,R)} \subset \mathbb{R}^d$ centered at $\mathbf{0}$ with radius R, Beurling's theorem tells us the following [3]: Let $\Lambda \subseteq \widehat{\mathbb{R}}^d$ be uniformly discrete and let $\text{dist}(\xi, \Lambda) = \inf_{\lambda \in \Lambda} \sqrt{\sum_{i=1}^d |\xi_i - \lambda_i|^2}$ denote the Euclidean distance between the point ξ and the set Λ. Define

$$\rho = \rho(\Lambda) = \sup_{\xi \in \widehat{\mathbb{R}}^d} \text{dist}(\xi, \Lambda).$$

If $R\rho < \frac{1}{4}$, then Λ is a Fourier frame for $PW_{\overline{B(0,R)}} \subseteq L^2(\widehat{\mathbb{R}}^d)$.

Define $L : L^2(E) \to \ell^2(\Lambda)$ of a Bessel map such that $f \to \{\widehat{f}(\lambda) : \lambda \in \Lambda\}$. Let L^* be its adjoint, and define the frame operator

$$S = L^* L : L^2(E) \to L^2(E)$$

such that $f \to S(f) = \sum_{\lambda \in \Lambda} \widehat{f}(\lambda) e_\lambda \mathbb{1}_E$. If $\{e_\lambda \mathbb{1}_E\}$ is a frame for $L^2(E)$, then

$$f = SS^{-1} f = \sum_{\lambda \in \Lambda} (S^{-1} f)^\wedge(\lambda) e_\lambda \mathbb{1}_E. \tag{1}$$

From this we can conclude that every finite energy signal $f \in L^2(E)$ can be represented as

$$f(x) = \sum_{\lambda \in \Lambda} a_\lambda(f) e_\lambda \mathbb{1}_E \tag{2}$$

in $L^2(\mathbb{R}^d)$, where $a_\lambda(f) = (S^{-1} f)^\wedge(\lambda)$ and $\sum_{\lambda \in \Lambda} |a_\lambda(f)|^2$ is finite.

Given the representation in (2), we must now choose a sequence $\Lambda_R \in \widehat{\mathbb{R}}^d$ such that Λ_R is a Fourier frame for $PW_{\overline{B(0,R)}}$. Let $c, R > 0$, and let $\{A_k : k = 0, 1, ..., m-1\}$ denote a finite set of interleaving Archimedean spirals of the form

$$A_k = \{c\theta e^{2\pi i(\theta - (k/m))} : \theta \geq 0\}.$$

Let $B = \cup_{k=0}^{m-1} A_k$. We will construct a uniformly discrete set $\Lambda_R \subseteq B$ that will form a Fourier frame for $PW_{\overline{B(0,R)}}$.

First, choose m such that $\frac{cR}{m} < 1/2$. For any given $\xi_0 \in \widehat{\mathbb{R}}^2$, we will write it as $\xi_0 = r_0 e^{2\pi i \theta_0}$ where $r_0 \geq 0$ and $\theta_0 \in [0, 1)$. Then either $0 \leq r_0 < c\theta_0 < c$ or there exists $n_0 \in \mathbb{N} \cup \{0\}$ for which

$$c(n_0 + \theta_0) \leq r_0 < c(n_0 + 1 + \theta_0).$$

In the second case, we can find $k \in \{0, \cdots, m-1\}$ such that

$$c(n_0 + \theta_0 + \frac{k}{m}) \leq r_0 < c(n_0 + \theta_0 + \frac{k+1}{m}),$$

which implies

$$\text{dist}(\xi_0, B) \leq \frac{c}{2m}.$$

Next, choose $\delta > 0$ such that $R\rho < 1/4$, where $\rho = (c/2m) + \delta$. For each k, we choose a uniformly discrete set of points Λ_k along the spiral A_k, where the curve distance between consecutive points is less than 2δ, beginning within 2δ of the origin. This rule guarantees that the distance from any point on the spiral A_k to Λ_k is less than δ. Finally, set $\Lambda_R = \cup_{k=0}^{m-1} \Lambda_k$. By the triangle inequality,

$$\begin{aligned} \forall \xi \in \widehat{\mathbb{R}}^2, \quad \text{dist}(\xi, \Lambda_R) &\leq \text{dist}(\xi, B) + \text{dist}(B, \Lambda_R) \\ &\leq \frac{c}{2m} + \delta = \rho. \end{aligned}$$

Recall that by our choices of δ and m, we have that $R\rho < 1/4$, thus Beurling's theorem tells us Λ_R is a Fourier frame for $PW_{\overline{B(0,R)}}$.

4 Problem

We shall extend the results in Section 3 to the signal space of a generic rectangular image $f : \mathbb{R}^2 \to \mathbb{R}$ in a space $E \subseteq \mathbb{R}^2$ [3]. Consider the image $f \in L^2(E)$, taken to be zero outside of E. Let $\chi_1 = \{\square_k^1, p_k \in \square_k^1 \ \forall k\}_{k=0}^{B-1}$ be a refined tagged partition of E. We approximate f using the piecewise constant function f_{χ_1} due to lack of access to real MRI data. This approximation incurs an error ϵ between the true, smooth image f and the image f_{χ_1}. However, for any choice of ϵ, we can refine χ_1 such that $||f - f_{\chi_1}|| < \epsilon$, thus f_{χ_1} is a reasonable approximation of f. For a high-resolution image, the pixels act as the partition χ_1. Under this partition, the image has the representation

$$f_{\chi_1} = \sum_{k=0}^{B-1} f(p_k) \mathbb{1}_{\square_k^1} \tag{3}$$

and the equivalent spectral representation

$$\widehat{f}_{\chi_1} = \sum_{k=0}^{B-1} f(p_k) \widehat{\mathbb{1}}_{\square_k^1}. \tag{4}$$

Let $\chi_2 = \{\square_j^2, q_j \in \square_j^2 \ \forall j\}_{j=0}^{N_1 N_2 - 1}$ be a coarse tagged partition of E such that f_{χ_2} is piecewise constant. χ_2 is designed such that for each $q_j \in \chi_2$, there is a corresponding $p_k \in \chi_1$. Ideally, we would recover f_{χ_2} from the spectral information $\widehat{f}$ from the MRI machine. Computationally, we reconstruct f_{χ_2} given $\widehat{f}_{\chi_1}$, the approximation of $\widehat{f}$.

We restrict our view of the spectral domain to the square $\Omega \subseteq \widehat{\mathbb{R}}^2$, where the frame contribution outside the square is negligible. From our theoretical results, we can choose a set of points $\Lambda \subseteq \widehat{\mathbb{R}}^2$ along a set of interleaving spirals that gives rise to a Fourier frame for $L^2(E)$. Within the restricted domain Ω, we choose $M \geq N_1 N_2$ points $\alpha_i = (\lambda_i, \mu_i)$ for $i = 0, 1, ..., M-1$ on the interleaving spirals such that the α_i are nonuniform in the square. Let $\Lambda = \{\alpha_i\}$. We extend this tiling to the entire spectral domain by utilizing the periodic extension $\Lambda + K\mathbb{Z}^2$, giving rise to a frame $\{e_{\alpha_i}\}_{\alpha_i \in \Lambda}$ for PW_E, where $E = [-\frac{1}{2}, \frac{1}{2}]^2$. By specifying the points $\alpha_i \in \Lambda \cap \Omega$, the MRI machine gives us access to $\{\widehat{f}_{\chi_1}(\alpha_i), i = 0, 1, ..., M-1\}$, the approximation of $\{\widehat{f}(\alpha_i)\}$, where we compute

$$\widehat{f}_{\chi_1}(\alpha_i) = \sum_{k=0}^{B-1} f(p_k) \widehat{\mathbb{1}}_{\square_k^1}(\alpha_i). \tag{5}$$

Let

$$g = \sum_{j=0}^{N_1 N_2 - 1} c_j \mathbb{1}_{\square_j^2} \tag{6}$$

be an image formed over the coarse partition χ_2. Given the spectral information $\widehat{f}_{\chi_1}(\alpha_i)$, we wish to find the image over the coarse partition that matches the frequency information of the high-resolution image at the points on the frame. To that end, we want to find c_j that solve

$$\min_c \sum_{i=0}^{M-1} |\widehat{f}_{\chi_1}(\alpha_i) - \widehat{g}(\alpha_i)|^2. \tag{7}$$

We then compare the actual recovered image g to the ideal recovered image f_{χ_2} formed by local averaging over the high-resolution image f_{χ_1}.

Let $H_j(\alpha_i) = \widehat{\mathbb{1}}_{\square_j^2}(\alpha_i)$. As the characteristic functions are separable by dimension, this is equivalent to $H_j(\alpha_i) = H_j(\lambda_i, \mu_i) = \widehat{\mathbb{1}}_{-\frac{2}{x_j}}(\lambda_i) \widehat{\mathbb{1}}_{-\frac{2}{y_j}}(\mu_i)$, where

$$H_j(\alpha_i) = H_j(\lambda_i, \mu_i) = \frac{1}{N_1} \frac{1}{N_2} \text{sinc}\left(\frac{1}{N_1} \lambda_i\right) \ \text{sinc}\left(\frac{1}{N_2} \mu_i\right) e^{-2\pi I (T_n \lambda_i + T_m \mu_i)} \tag{8}$$

We define $\text{sinc}(x)$ as the standard $\text{sinc}(x) = \frac{\sin \pi x}{\pi x}$, with sinc(0)=1, and (T_n, T_m) as the coordinates of the center of the current square, with $T_n = -\frac{1}{2} + \frac{2n+1}{2N_1}$ for $n \in \{0, ..., N_1 - 1\}$ and $T_m = -\frac{1}{2} + \frac{2m+1}{2N_2}$ for $m \in \{0, ..., N_2 - 1\}$. This gives

$$\widehat{g}(\alpha_i) = \sum_{j=0}^{N_1 N_2 - 1} c_j H_j(\alpha_i). \tag{9}$$

To minimize $|\widehat{f}_{\chi_1}(\alpha_i) - \widehat{g}(\alpha_i)|^2$, we set

$$\widehat{f}_{\chi_1}(\alpha_i) = \sum_{j=0}^{N_1 N_2 - 1} c_j H_j(\alpha_i). \tag{10}$$

Let

$$\widehat{\mathbb{F}} = [\widehat{f}_{\chi_1}(\alpha_0)\ \widehat{f}_{\chi_1}(\alpha_1)\ ...\ \widehat{f}_{\chi_1}(\alpha_{M-1})]^{\mathrm{T}}$$

and

$$\mathbb{F} = [c_0\ c_1\ ...\ c_{N_1 N_2 - 1}]^{\mathrm{T}}.$$

Define $\mathbb{H}$ such that $[\mathbb{H}]_{i,j} = H_j(\alpha_i)$, and (10) becomes

$$\widehat{\mathbb{F}} = \mathbb{H}\mathbb{F}. \tag{11}$$

Recall that for effective reconstruction, we must have $M \geq N_1 N_2$, thus we will find the least squares approximation of the overdetermined system in (11). The matrix equation (11) contains $M \geq N_1 N_2$ points in the spectral domain and $N_1 N_2$ points in the spatial domain. $\widehat{\mathbb{F}}$ is a length-M vector, $\mathbb{F}$ is a length-$N_1 N_2$ vector, and $\mathbb{H}$ is size $M \times N_1 N_2$. In the following section, we will show that this matrix representation is equivalent to the frame reconstruction scheme.

5 Frame Reconstruction

The goal of this project is to use nonuniform sampling on interleaving spirals to define a Fourier frame in $\widehat{\mathbb{R}}^2$ from which we can reconstruct an image f. Due to the lack of access to real MRI data, we use the spectral information over the fine partition χ_1 to recover the spatial components of our image f over a coarse partition χ_2. We create a synthetic data set using high-resolution images.

Given a high resolution image f_{χ_1}, generally of size 512×512, we form f_{χ_2}, an $N_1 \times N_2$ approximant, by averaging every $d_1 \times d_2$ pixels of f_{χ_1}, where d_1 and d_2 are the reduction factors in each dimension. The $N_1 \times N_2$ approximant f_{χ_2} is the optimal available image at that resolution. We take this as our ideal reconstruction, from which the error is computed. From the high-resolution image f_{χ_1}, we sample $\widehat{f}_{\chi_1}(\alpha_i)$ as defined in (5) for $i = 0, 1, ..., M - 1$ (with $M \geq N_1 N_2$) on a union of Archimedean spirals within the square Ω (Figure 5.1).

Beurling's theorem allows us to develop a reconstruction scheme using the set of points $\Lambda = \{\alpha_i\}$. The frame definition gives rise to a mapping $\mathbb{H}$ of $N_1 N_2$ points to M points, thus $\mathbb{H}$ is the matrix representation of the Bessel map $L : \ell^2(\{0, 1, ..., N_1 N_2 - 1\}) \to \ell^2(\{0, 1, ..., M - 1\})$, $\mathbb{H}^*$ is its adjoint L^*, and $\mathbb{H}^*\mathbb{H}$ is equivalent to the frame operator $S = L^* L$. The frame reconstruction scheme is

$$g = (S^{-1} L^*) L g. \tag{12}$$

Setting $Lg = \widehat{f}_{\chi_1}$, the reconstructed image g takes the form

$$g = S^{-1} L^* \widehat{f}_{\chi_1}. \tag{13}$$

Applying the construction in Section 4 yields the overdetermined system in (11). In frame terminology, the least-squares approximation

$$\mathbb{F} = (\mathbb{H}^*\mathbb{H})^{-1}\mathbb{H}^*\widehat{\mathbb{F}}, \tag{14}$$

where $\mathbb{H}^* := \overline{\mathbb{H}}^{\mathrm{T}}$, is equivalent to (12).

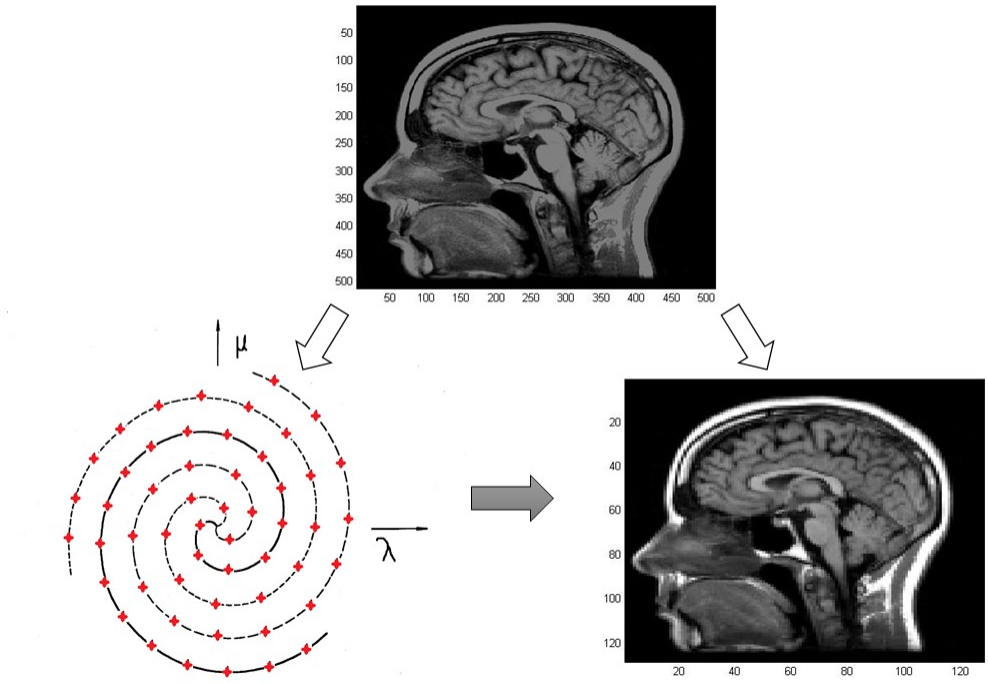

Figure 5.1: Problem overview. Top: High-resolution image f_{χ_1} from which synthetic data is formed. Bottom left: Sampling along interleaving spirals in the spectral domain of the high-resolution image. Bottom right: Downsampled version of the high-resolution image that serves as the ideal reconstruction.

6 Computational Approach

We wish to recover g by constructing $\widehat{\mathbb{F}}$ and $\mathbb{H}$ as described Section 4. We consider both the LDL decomposition, a variant on Cholesky decomposition, and the conjugate gradient method to solve the system

$$\mathbb{H}^*\mathbb{H}\mathbb{F} = \mathbb{H}^*\widehat{\mathbb{F}}. \tag{15}$$

To reduce the storage overhead, we also implement the transpose reduction algorithm.

6.1 Transpose Reduction

Transpose reduction computes $\mathbb{H}^*\mathbb{H}$ directly as a sum of vector products instead of inefficiently storing $\mathbb{H}$ and then computing $\mathbb{H}^*\mathbb{H}$ [3, 8]. Define $V_i = (H_0(\alpha_i), ..., H_{N_1N_2-1}(\alpha_i))^*$ such that

$$\mathbb{H} = \begin{pmatrix} H_0(\alpha_0) & \cdots & H_{N_1N_2-1}(\alpha_0) \\ H_0(\alpha_1) & \cdots & H_{N_1N_2-1}(\alpha_1) \\ \vdots & \vdots & \vdots \\ H_0(\alpha_{M-1}) & \cdots & H_{N_1N_2-1}(\alpha_{M-1}) \end{pmatrix} = \begin{pmatrix} V_0^* \\ V_1^* \\ \vdots \\ V_{M-1}^* \end{pmatrix}.$$

Note that

$$\begin{aligned}
\mathbb{H}^*\mathbb{H} &= \begin{pmatrix} \sum_{i=0}^{M-1} \overline{H_0(\alpha_i)} H_0(\alpha_i) & \cdots & \sum_{i=0}^{M-1} \overline{H_0(\alpha_i)} H_{N_1N_2-1}(\alpha_i) \\ & \vdots & \\ \sum_{i=0}^{M-1} \overline{H_{N_1N_2-1}(\alpha_i)} H_0(\alpha_i) & \cdots & \sum_{i=0}^{M-1} \overline{H_{N_1N_2-1}(\alpha_i)} H_{N_1N_2-1}(\alpha_i) \end{pmatrix} \\
&= \sum_{i=0}^{M-1} \begin{pmatrix} \overline{H_0(\alpha_i)} H_0(\alpha_i) & \cdots & \overline{H_0(\alpha_i)} H_{N_1N_2-1}(\alpha_i) \\ & \vdots & \\ \overline{H_{N_1N_2-1}(\alpha_i)} H_0(\alpha_i) & \cdots & \overline{H_{N_1N_2-1}(\alpha_i)} H_{N_1N_2-1}(\alpha_i) \end{pmatrix} \\
&= \sum_{i=0}^{M-1} \begin{pmatrix} \overline{H_0(\alpha_i)} \\ \overline{H_1(\alpha_i)} \\ \vdots \\ \overline{H_{N_1N_2-1}(\alpha_i)} \end{pmatrix} (H_0(\alpha_i)\ H_1(\alpha_i)\ \cdots\ H_{N_1N_2-1}(\alpha_i)) \\
&= \sum_{i=0}^{M-1} V_i V_i^*.
\end{aligned}$$

Similarly,

$$\mathbb{H}^*\widehat{\mathbb{F}} = \begin{pmatrix} \sum_{i=0}^{M-1} \overline{H_0(\alpha_i)} \widehat{\mathbb{F}_i} \\ \vdots \\ \sum_{i=0}^{M-1} \overline{H_{N_1N_2-1}(\alpha_i)} \widehat{\mathbb{F}_i} \end{pmatrix} = \sum_{i=0}^{M-1} \widehat{\mathbb{F}_i} V_i.$$

To construct $A = \mathbb{H}^*\mathbb{H}$ and $b = \mathbb{H}^*\widehat{\mathbb{F}}$:

1. Let $V_0 = (H_0(\alpha_0), ..., H_{N_1N_2-1}(\alpha_0))^*$
2. Set $A = V_0V_0^*$ and $b = \widehat{f_0}V_0$
3. For $j = 1 : M-1$

   Set $V_j = (H_0(\alpha_j), ..., H_{N_1N_2-1}(\alpha_j))^*$
   $A \leftarrow A + V_jV_j^*$
   $b \leftarrow b + \widehat{f_j}V_j$

This method uses a factor of N^2/M less memory than the direct approach with naive storage.

6.2 Conjugate Gradient Algorithm

Given the construction of $\mathbb{H}^*\mathbb{H}$,

$$[\mathbb{H}^*\mathbb{H}\mathbb{F}]_\ell = \sum_{j=0}^{N_1N_2-1} \mathbb{F}_j \sum_{i=0}^{M-1} \overline{H_\ell(\alpha_i) H_j(\alpha_i)},$$

where $[\mathbb{H}^*\mathbb{H}\mathbb{F}]_\ell$ denotes the ℓth element of $\mathbb{H}^*\mathbb{H}\mathbb{F}$. As in the Transpose Reduction algorithm, let $A = \mathbb{H}^*\mathbb{H}$ and $b = \mathbb{H}^*\widehat{\mathbb{F}}$. Then, for symmetric, positive definite A, we apply the conjugate gradient method [10] to solve the system $A\mathbb{F} = b$.

1. Choose f_0. Let $r_0 = b - Af_0$. Set $p_0 = r_0$.
2. for $n = 1$ until convergence

   $\gamma = (r_n^T r_n)/((Ap_n)^T p_n)$
   $f_{n+1} = f_n + \gamma p_n$

$r_{n+1} = r_n - \gamma A p_n$
if norm$(r_{n+1}) <$ tol, break
$\beta_n = (r_{n+1}^T r_{n+1})/(r_n^T r_n)$
$p_{n+1} = r_{n+1} + \beta_n p_n$

This algorithm requires at most $N_1 N_2$ iterations to converge, but the speed of convergence depends on the condition number of A. We also develop a modified implementation of the conjugate gradient algorithm that uses only matrix-vector operations instead of explicitly storing A.

7 Validation

Validation is done in two parts. First, an image is reconstructed over a standard uniform (rectilinear) sampling in the spectral domain using both reconstruction methods. Uniform reconstruction verifies correct implementation of the reconstruction algorithms. Reconstruction along the spiral is shown for a 2x2 image to validate the implementation of the theoretical framework presented in Section 3.

The use of a complex system to represent a real system creates an expectation of noise in the reconstruction in the form of non-zero imaginary components. Despite this, as the coefficients of the reconstruction should be real, we expect those imaginary components to be small. Indeed, we see that increasing the number of sampled points M significantly reduces the imaginary components to the point where their contribution is negligible. Thus, when discussing results, we only discuss those taken from the real components of the linear system and ignore the contribution of the imaginary components. In each result, the imaginary components are monitored to ensure their contribution remains trivial.

7.1 Validation Methods

Results shown are evaluated using two different measures, the peak signal-to-noise ratio (PSNR) [7] and the structural similarity index (SSIM) [11].

7.1.1 Peak Signal-to-Noise Ratio (PSNR)

PSNR is a standard measure of a reconstructed image that calculates a normalized mean-squared error expressed in decibels (dB). Given the optimal available image f_{χ_2} of dimension $N_1 \times N_2$ and the reconstructed image g,

$$MSE = \frac{1}{N_1 N_2} \sum_{m=0}^{N_1-1} \sum_{n=0}^{N_2-1} (g(m,n) - f_{\chi_2}(m,n))^2$$

Then the PSNR, expressed in decibels (dB), is

$$PSNR = 10 \log \frac{max_{f_{\chi_2}}^2}{MSE} \tag{16}$$

where $max_{f_{\chi_2}}$ is the maximum possible pixel value for f_{χ_2}. As purely grayscale images are used for this project, $max_{f_{\chi_2}} = 255$.

7.1.2 Structural Similarity Index (SSIM)

The structural similarity (SSIM) index is a statistical measure of similarity between two images based on inherent structures [11]. SSIM ranges from zero to one, with a value close to one indicating a good match. Let x and y be signals where one is assumed to be of perfect quality. The luminance of each image is estimated by the mean intensities μ_x and μ_y. The standard deviations σ_x and σ_y are used to estimate the signal contrast. The constants C_1 and C_2 are used as stabilizers for when $\mu_x^2 + \mu_y^2$ and $\sigma_x^2 + \sigma_y^2$ are close to zero. The final form of the SSIM index is

$$\text{SSIM}(x,y) = \frac{(2\mu_x\mu_y + C_1)(2\sigma_{xy} + C_2)}{(\mu_x^2 + \mu_y^2 + C_1)(\sigma_x^2 + \sigma_y^2 + C_2)},$$

7.2 Uniform Grid Reconstruction

To validate the code structure, we first reconstruct an image over a uniform grid. The grid consists of the integers in the spectral domain ranging from [-floor($\sqrt{M}$)/2, floor($\sqrt{M}$)/2]^2, where M is the desired number of sampled points. In this test, the grid contains twice as many sampled points from the high-resolution image as there are pixels in the reconstruction. Figure 7.1 shows the recovered images for both LDL reconstruction and conjugate gradient reconstruction. The conjugate gradient method requires 10 iterations for convergence within relative tolerance 1e-8 $||\mathbb{H}^*\widehat{\mathbb{F}}||$. Reconstruction via the real components of the resulting coefficients produces the expected result with high PSNR of 29.12 dB and SSIM of 0.9895. The largest imaginary component of the recovered image is 2.4. Consistently, comparison with the image recovered by incorporating the imaginary components reveals similar PSNR and SSIM, indicating minimal contribution from the imaginary components. In every test, the LDL decomposition and the conjugate gradient method returned the same result, thus further tests do not distinguish between the two methods used in the recovery.

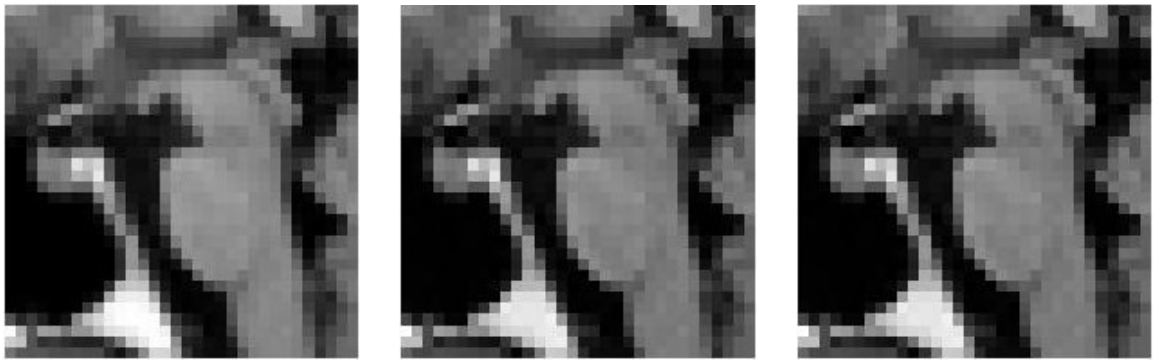

Figure 7.1: Uniform grid reconstruction along integers in the domain [-floor($\sqrt{M}$)/2, floor($\sqrt{M}$)/2]^2, $M = 2048$ (oversampling factor of 2). Ideal reconstruction (L), reconstruction via LDL decomposition (M), reconstruction via CG method (R), $N_1 = N_2 = 32$. PSNR: 29.12 dB, SSIM: 0.9895.

7.3 Spiral Grid Reconstruction

To validate reconstruction on the spiral, a 2x2 low-resolution image is reproduced from high-resolution images of varying size. The frame Λ is generated from three spirals with $\lambda = 0.01$ radians and consists of the points in Table 7.1.

Real(α_i)	Imag(α_i)
0	0
0.0005	0.0002
0.0100	0.0006
0.0149	0.0014
0.0198	0.0025
0.0247	0.0039
0.0295	0.0056
0.0342	0.0076

Table 7.1: Frame Λ for 2x2 reconstruction test along the spiral.

The results of reconstructing the image from a 16x16 high-resolution image are shown in Figure 7.2, with the accompanying details in Table 7.2. This example showcases a reduction by a factor of eight in each dimension with a PSNR of 33.3959 dB and SSIM 0.9454. Average error, defined in (17), is calculated as the

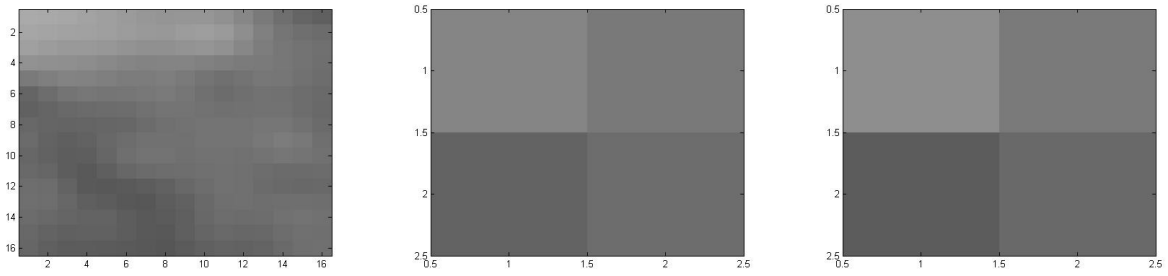

Figure 7.2: 2x2 reconstruction test along the spiral with $M = 8$ points in the frame (oversampling factor of 2), $\theta = 0.01$, $m = 3$ interleaving spirals. L: 16x16 high-resolution image. M: Ideal image. R: Recovered image. $N_1 = N_2 = 2$. PSNR: 33.3959 dB, SSIM: 0.9454.

HR Image Size	PSNR (dB)	SSIM	Avg. Err. Per Pixel
4x4	39.5274	0.9681	1.25
8x8	33.6982	0.9739	2.5
16x16	33.3959	0.9454	2.75
32x32	30.3132	0.9288	3.25
64x64	32.9457	0.9586	2.5
128x128	23.8535	0.6116	8.0
256x256	32.9457	0.9633	2.5

Table 7.2: 2x2 recovery test on the spiral grid. High-resolution images of various sizes are used to reconstruct a 2x2 image.

mean of the 1-norm of the differences between corresponding pixels of the ideal and recovered image. The average error per pixel stays within 4% of the ideal value.

$$\text{Avg. err. per pixel} = \frac{1}{N_1 N_2} \sum_{j=0}^{N_1 N_2 - 1} |f_{\chi_2}(q_j) - g(c_j)| \tag{17}$$

In total, seven tests were conducted, where a 2x2 image was reconstructed from high-resolution images of sizes $2^k \times 2^k$ for $k \in \{2, ...8\}$. Table 7.2 describes the results. Note that PSNR and SSIM both remain high for most tests, indicating good recovery significantly above the noise floor. There is one anomaly in the recovery from the 128x128 high-resolution image, but the accompanying PSNR of 23.85 dB matches the expected PSNR of a noisy image. Similarly, the SSIM of 0.6116 indicates that while the recovery here is poor relative to the other tests, the resulting image still shows some structure. Ultimately, the recovery seems to be hampered by some type of noise. The source of this noise is uncertain, but it likely comes from the structures in the high-resolution image that are changing as the size of the high-resolution image increases.

8 Testing

The frame Λ is formed using the experimental parameters $c = 1$, and $R = 0.5\frac{\sqrt{2}}{2}$. It samples $K \times N_1 \times N_2$ points in the spectral domain. Unless otherwise specified, the points in the frame are chosen along $m = 3$ spirals.

8.1 Oversampling Factor

The effectiveness of the reconstruction on the spiral primarily depends on two parameters, the number of points that make up the frame and the polar angle of the spiral. Beginning with a 128x128 high-resolution

image, low-resolution images are recovered from frames of varying size while holding the spiral angle constant at $\theta = 0.01$ radians. For each image, the number of desired points is $M = K \times N_1 \times N_2$, where $K \in \mathbb{N}$ is the oversampling factor. Table 8.4 suggests altering the parameter K has a significant impact on the recovery.

Recovered image size	K	PSNR (dB)	SSIM	Avg. Err. Per Pixel
8x8	16	17.8413	0.8035	13.9844
8x8	32	26.9622	0.9690	4.0312
16x16	8	11.8310	0.2899	17.0976
16x16	16	29.8072	0.9900	6.1992
32x32	4	8.6455	0.0131	69.5225
32x32	8	27.3753	0.9875	9.2764

Table 8.1: Oversampling factor K reconstruction test along the spiral.

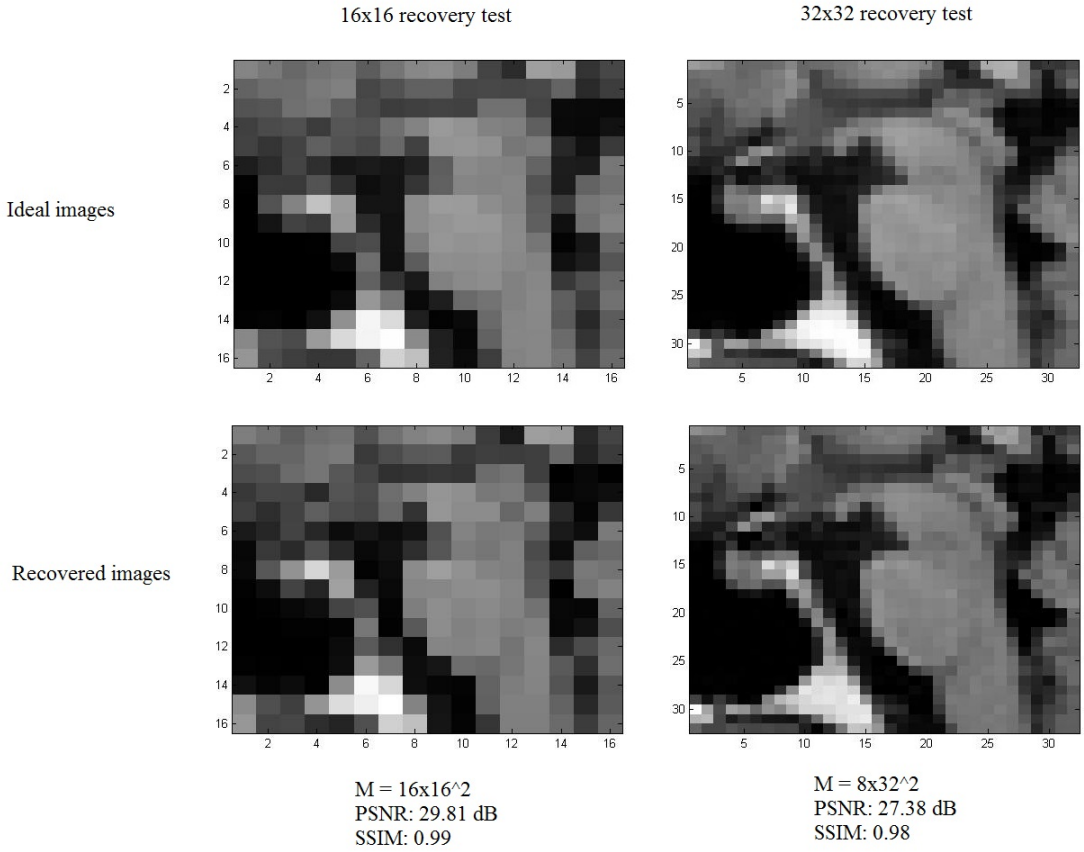

Figure 8.1: Oversampling factor K reconstruction test along the spiral. High-resolution image size 128x128, $\theta = 0.01$, $m = 3$. Twice as many samples are required to reconstruct the 32x32 image.

More comprehensive testing shows an apparent plateau in the reconstruction, suggesting there is a minimum value of K that will adequately reconstruct the desired image for a given image size $N_1 \times N_2$. More samples (a larger K value) are required to reconstruct a larger image with comparable PSNR and SSIM values (Figure 8.1). The 8x8 recovery results are shown in Figure 8.2, where the angle of the spiral is held constant and K varies between 1 and 32. The maximum imaginary component decreases to 0.53 for $K = 32$. The advantage of the ability to determine the minimum number of sampled points is twofold: it allows for acceptable error thresholding and it reduces computational time.

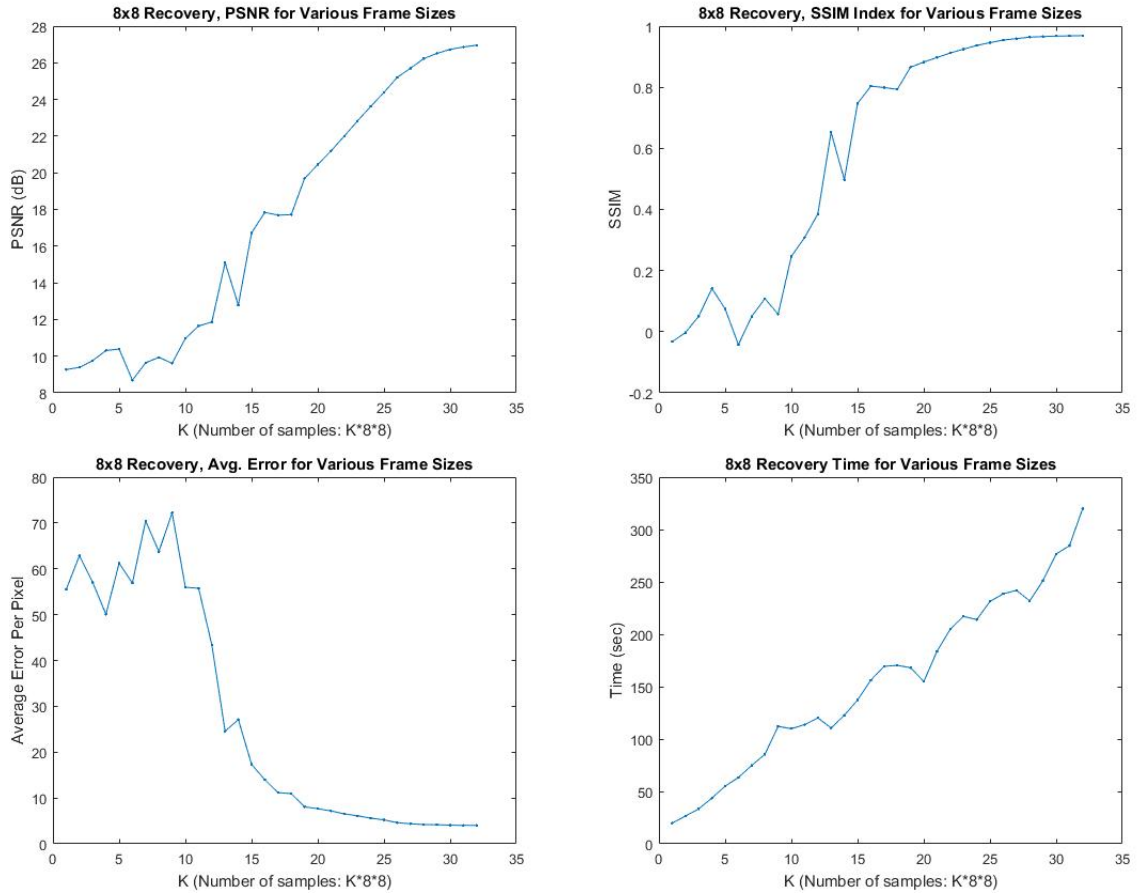

Figure 8.2: Reconstruction test varying oversampling factor K, $\theta = 0.01$, $m = 3$. High-resolution image size 128x128. Top: PSNR and SSIM for varying K in 8x8 low-resolution reconstruction. Bottom: Average error per pixel and run time for varying K.

8.2 Spiral Angle

The tightness of the spiral is determined by its polar angle θ. The results of recovering an 8x8 low-resolution image for varying θ values while holding $K = 30$ constant are shown in Figure 8.3. Despite comparable PSNR values for multiple values of θ, a close examination reveals that SSIM decreases as θ increases. Similar to the choice of oversampling factor, this suggests there is a range of acceptable values of θ that will produce an effective reconstruction for the given set of problem parameters. If chosen effectively, the angle of the spiral has less of an effect on the reconstruction than the number of samples in the spectral domain. This is reflected in the number of points sampled in the restricted domain as Ω is held constant. As θ increases, the number of sampled points M decreases, with less effective corresponding reconstructions.

8.3 Oasis Database

To test the robustness of the reconstruction, several images were reconstructed from the open-source Oasis database. The database is provided by Washington University Alzheimer's Disease Research Center, Dr. Randy Buckner at the Howard Hughes Medical Institute (HHMI) at Harvard University, the Neuroinformatics Research Group (NRG) at Washington University School of Medicine, and the Biomedical Informatics Research Network (BIRN). The full data set contains 416 subjects aged 18 to 96, 100 of whom have varying levels of Alzheimer's disease. A subset of these individuals containing 39 subjects was used for this test. Multiple scans are provided for each subject. Here, the high-resolution images shown are averages of four scans

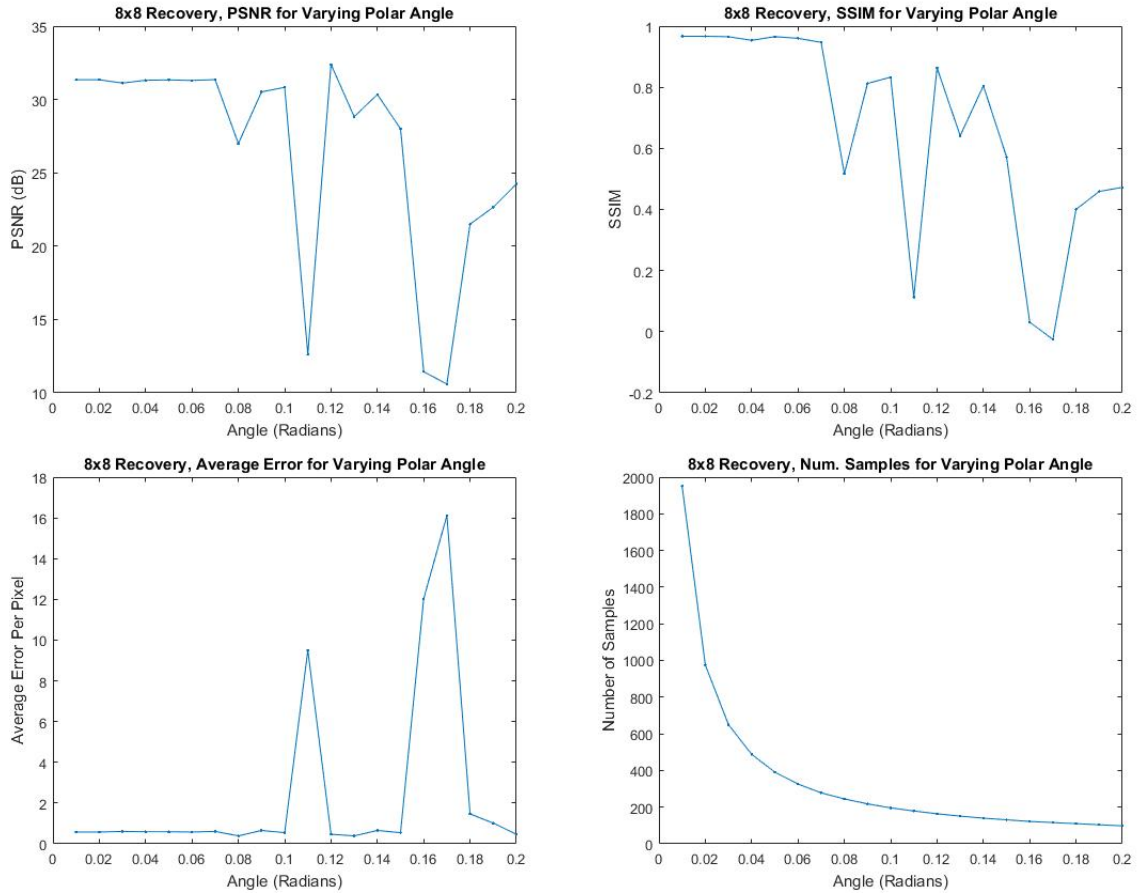

Figure 8.3: Reconstruction test varying polar angle θ, $m = 3$. Top: PSNR and SSIM for varying θ in 8x8 low-resolution reconstruction. Bottom: Average error per pixel and number of samples for varying θ.

per subject with postprocessing applied. Among the subjects in the testing set, there are twenty-two females and seventeen males. Nine of these subjects have very mild dementia and three subjects have mild dementia. The Oasis database diagnoses every subject with any presence of dementia with probable Alzheimer's disease. Results for three subjects are shown in Figure 8.4. The left column displays an 80-year-old male with very mild dementia, the center column an 80-year-old female with very mild dementia, and the right column an 18-year-old male with no dementia. The results suggest our parameters are independent of the image we are trying to recover.

8.4 Further Observations

Image size (N_1xN_2)	cond($\mathbb{H}^*\mathbb{H}$)	LDL time (s)	CG time (s)	Num. CG iter.
2x2	4.33	9.64e-4	2.265e-3	4
4x4	11.40	1.55e-4	1.132e-3	16
8x8	24.94	4.10e-4	1.484e-2	26
16x16	51.43	2.45e-2	7.655e-3	39
32x32	103.78	6.00e-1	1.441e-1	51

Table 8.2: Method comparison for recovery of images of varying size.

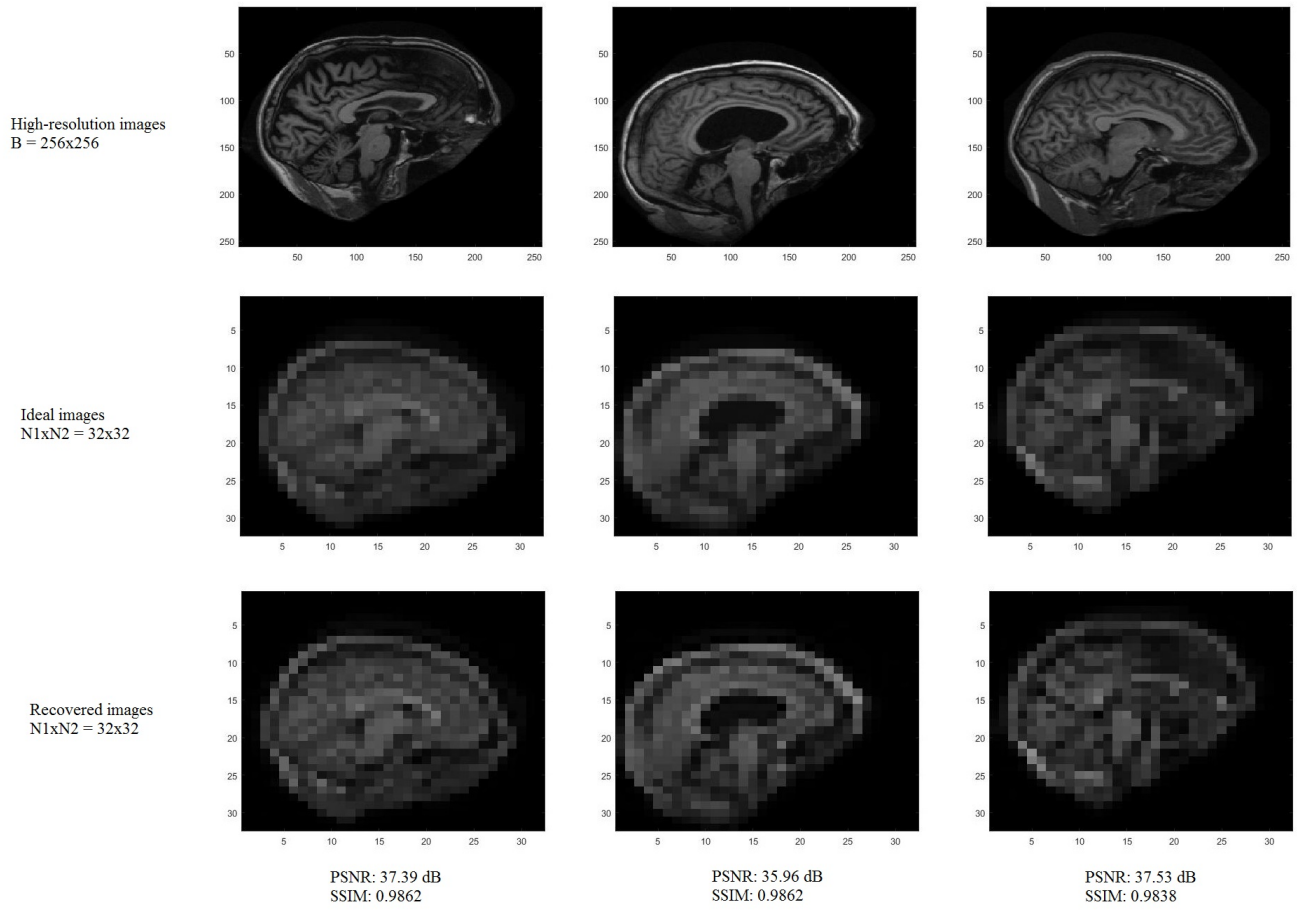

Figure 8.4: Oasis reconstruction test, $K = 8$, $\theta = 0.01$, $m = 3$.

As noted earlier, the distinction between recovery from the LDL decomposition versus the conjugate gradient (CG) method is neglected since the methods return the same result to machine precision. If the reconstruction requires a less strict error threshold, the threshold in the CG method can be adjusted for faster convergence. Ultimately, the CG method may be preferred due to its ability to handle linear systems with large condition numbers. Table 8.2 shows that the condition number of the system doubles with each increase in the size of the recovered image. In each case, the number of sampled points used to obtain the recovered image also doubles, indicating there may be a correlation between the condition number of the system and the frame size. From a timing perspective, the methods are comparable. Most of the timing overhead in these tests comes from the formation of $\widehat{\mathbb{F}}$. In a real setting, the MRI machine would collect the data, making this construction unnecessary.

8.5 Future Work

The relationship between the condition number of the system and the frame size needs to be further explored. The behavior in Figure 8.2 suggests that theoretical bounds can be established in the choice of parameter values. In addition, a larger number of sampled points indicates a larger sample domain Ω. The relationship between the oversampling factor and the corresponding size of Ω can be more firmly established. The behavior in Figure 8.3 leaves room for exploration as to the oscillatory nature of the results. This behavior was consistent across multiple images, suggesting that careful construction of the spiral is essential to the reconstruction process.

9 Conclusion

We have shown that we can effectively reconstruct an MRI image from nonuniform spectral information sampled along a set of interleaving Archimedean spirals. The reconstruction is robust across different images when the oversampling factor K and the polar angle θ are chosen in a reasonable range. Despite the increasing oversampling factor, this implementation is easily parallelizable, suggesting this reconstruction method is feasible in a real setting.

10 Milestones

- Construct a Fourier frame via sampling on interleaving spirals.
- Implement the transpose reduction algorithm.
- Implement the conjugate gradient algorithm.
- Implement the vectorized conjugate gradient algorithm.

11 Timeline

- October 2015: Code the sampling routine to form the Fourier frame. [**Complete**]
- November 2015: Validation on small problems. [**Complete**]
- December 2015: Code the transpose reduction algorithm and begin testing. [**Complete**]
- January 2016: Code the conjugate gradient algorithm (standard and modified). [**Complete**]
- February - March 2016: Error analysis/testing. [**Complete**]
- April 2016: Finalize results. [**Complete**]

12 Deliverables

- Oasis data set
- Downsampling routine
- Fourier frame sampling routine
- Conjugate gradient routine
- Main driver
- Proposal presentation and report
- Mid-year presentation and report
- Final presentation and report

References

[1] Au-Yeung, Enrico, and John J. Benedetto. "Generalized Fourier Frames in Terms of Balayage." Journal of Fourier Analysis and Applications 21.3 (2014): 472-508.

[2] Benedetto, John J., and Hui C. Wu. "Nonuniform Sampling and Spiral MRI Reconstruction." Wavelet Applications in Signal and Image Processing VIII (2000).

[3] Benedetto, John J., Alfredo Nava-Tudela, Alex Powell, and Yang Wang. MRI Signal Reconstruction by Fourier Frames on Interleaving Spirals. Technical report. 2008.

[4] Berger, Abi. "Magnetic Resonance Imaging." BMJ : British Medical Journal. BMJ, 5 Jan. 2002. Web. 13 Oct. 2015.

[5] Bloch F. "Nuclear induction." Physical Review (1946):460-474.

[6] Bourgeois, Marc, Frank T. A. W. Wajer, Dirk Van Ormondt, and Danielle Graveron-Demilly. "Reconstruction of MRI Images from Non-Uniform Sampling and Its Application to Intrascan Motion Correction in Functional MRI." Modern Sampling Theory (2001): 343-63.

[7] I. Daubechies. *Ten Lectures on Wavelets*. Society for Industrial and Applied Mathematics, Philadelphia, PA, 1992.

[8] Goldstein, Thomas, Gavin Taylor, Kawika Barabin, and Kent Sayre. "Unwrapping ADMM: Efficient Distributed Computing via Transpose Reduction." Sub. 8 April 2015.

[9] Mansfield, P. "Multi-planar Image Formation Using NMR Spin Echoes." J. Phys. C: Solid State Phys. Journal of Physics C: Solid State Physics 10.3 (1977).

[10] O'Leary, Dianne P. Scientific Computing with Case Studies. Philadelphia: Society for Industrial and Applied Mathematics, 2009.

[11] Wang, Z., A.C. Bovik, H.R. Sheikh, and E.P. Simoncelli. "Image Quality Assessment: From Error Visibility to Structural Similarity." IEEE Transactions on Image Processing IEEE Trans. on Image Process. 13.4 (2004): 600-12.

[12] Yan, Hong. Signal Processing for Magnetic Resonance Imaging and Spectroscopy. New York: Marcel Dekker, 2002.

[13] "Magnetic Resonance Imaging (MRI)." Magnetic Resonance Imaging (MRI). NIH. Web. 13 Oct. 2015.